Chapter 2
Simulation Techniques

An often used method to produced turbulence in numerical simulations is random forcing. Although this method is a mathematical idealization, it allows us to perform numerical experiments in the sense that a statistically stationary and isotropic turbulent state is prepared, with well defined statistical properties that can be compared to analytical theories. For more realistic astrophysical applications, adaptive methods are indispensable. Adaptive mesh refinement was introduced to efficiently treat flows with inhomogeneous structure. The basic idea is that the numerical resolution is dynamically adjusted such that subregions of the flow with strong fluctuations or steep gradients are well resolved, while smoother regions are covered by relatively coarse grids. The treatment of turbulent flows with adaptive mesh refinement, however, is still a challenging problem, mainly because refinement criteria that are sensitive to turbulent eddies or shocks in supersonic turbulence are difficult to formulate. The need to fully resolve turbulence, however, might be ameliorated by subgrid scale models, which approximate the effect of numerically unresolved turbulent eddies and shocks through turbulent viscosity and pressure in large eddy simulations.

2.1 Turbulence Forcing

There is a long record of turbulence simulations in astrophysics, where a force density $\rho\mathbf{f}$ in Eqs. (1.2) and (1.3) smoothly accelerates the fluid on large scales (in the context of the ISM, examples are [1–12]). One method is to use a spatially random static pattern, for which the amplitude is adjusted for each numerical time step so that power of the forcing is approximately constant [13, 14]. To produce statistically homogeneous and isotropic turbulence, it is advantageous to compose the force from randomly evolving Fourier modes. Each mode is given by a stochastic process of a particular type, the so-called *diffusion process*. A random variable $\mathscr{U}_t$ that evolves as a diffusion process in time is determined by a drift coefficient $a(\mathscr{U}_t, t)$ and a diffusion coefficient $b(\mathscr{U}_t, t)$. A fundamental diffusion process with Gaussian statistics is the

W. Schmidt, *Numerical Modelling of Astrophysical Turbulence*,
SpringerBriefs in Astronomy, DOI: 10.1007/978-3-319-01475-3_2,

Wiener process, for which $a(\mathscr{U}_t, t) = 0$ and $b(\mathscr{U}_t, t) = 1$. The time evolution of this process is defined by infinitesimal increments

$$\mathrm{d}\mathscr{W}_t = \mathscr{W}_{t+\mathrm{d}t} - \mathscr{W}_t = \mathscr{N}(0, \mathrm{d}t), \tag{2.1}$$

where $\mathscr{N}(0, \mathrm{d}t)$ is a normal distribution with mean zero and standard deviation equal to the time increment $\mathrm{d}t$. From the Wiener process, a statistically stationary diffusion process can be constructed by defining

$$a(\mathscr{U}_t, t) = -\frac{\mathscr{U}_t}{t}, \quad b^2(\mathscr{U}_t, t) = \frac{2\sigma^2}{T}. \tag{2.2}$$

This results in a Langevin-type stochastic differential equation:

$$\mathrm{d}\mathscr{U}_t = a(\mathscr{U}_t, t)\mathrm{d}t + b(\mathscr{U}_t, t)\mathrm{d}\mathscr{W}_t = -\mathscr{U}_t \frac{\mathrm{d}t}{T} + \left(\frac{2\sigma^2}{T}\right)^{1/2} \mathrm{d}\mathscr{W}_t. \tag{2.3}$$

The stochastic process $\mathscr{U}_t$ given by this equation is known as *Ornstein-Uhlenbeck process*.

The mean of $\mathscr{U}_t$ is given by $\langle \mathscr{U}_t \rangle = \langle \mathscr{U}_0 \rangle e^{-t/T}$. Therefore, any information about the initial configuration is exponentially damped over the autocorrelation time scale T. The variance is determined by the differential equation

$$\frac{\mathrm{d}}{\mathrm{d}t}\langle \mathscr{U}_t^2 \rangle = \frac{2}{T}\left(-\langle \mathscr{U}_t^2 \rangle + \sigma^2\right), \tag{2.4}$$

which has the solution

$$\langle \mathscr{U}_t^2 \rangle = \sigma^2 + \left(\langle \mathscr{U}_0^2 \rangle - \sigma^2\right) e^{-2t/T}. \tag{2.5}$$

If $\langle \mathscr{U}_0^2 \rangle = \sigma^2$, then $\langle \mathscr{U}_t^2 \rangle = \sigma^2$ for all t. Otherwise, the deviation of $\langle \mathscr{U}_t^2 \rangle$ from σ^2 is exponentially damped. Hence, the Ornstein-Uhlenbeck process is *asymptotically stationary* with $\langle \mathscr{U}_\infty^2 \rangle = \sigma^2$. Numerically, the process is readily implemented via the conditional distribution function

$$F(\mathscr{U}_2; t_2 | \mathscr{U}_1; t_1) = \mathscr{N}\left(\mathscr{U}_1 \mathrm{e}^{-(t_2 - t_1)/T}, \sigma^2\left[1 - \mathrm{e}^{-2(t_2 - t_1)/T}\right]\right). \tag{2.6}$$

Now, we can define the Fourier modes $\widehat{\mathbf{f}}(\mathbf{k}, t)$ of the acceleration field in terms of the Ornstein-Uhlenbeck process [8, 15, 16]:

$$\mathrm{d}\widehat{\mathbf{f}}(\mathbf{k}, t) = g_\zeta \left[-\widehat{\mathbf{f}}(\mathbf{k}, t)\frac{\mathrm{d}t}{T} + \frac{V}{T}\left(\frac{2\sigma^2(\mathbf{k})}{T}\right)^{1/2} \mathbf{P}_\zeta(\mathbf{k}) \cdot \mathrm{d}\mathscr{W}_t\right], \tag{2.7}$$

where it is understood that $\mathscr{W}_t$ is a vector of three statistically independent Wiener processes. Of course, we also assume that all Fourier modes are given by independent diffusion processes. The normalization coefficient g_ζ and the projection operator $\mathbf{P}_\zeta(\mathbf{k})$ are defined below. The autocorrelation time scale T of the forcing is identified with the large-eddy turn-over time $T = L/V$, where V is the characteristic velocity of the flow, and the integral length $L = X/\alpha$ is set to a fraction $1/\alpha$ of the domain size X. The stochastic diffusion term in Eq. (2.7) ensures that the resulting force field becomes statistically isotropic in physical space, while the drift term causes any anisotropic initial condition to dacay exponentially. This is not guaranteed with the method of steady random forcing, where isotropy must be prepared to very high precision in the initial velocity field.

Ideally, one would choose $\alpha \ll 1$ in order to minimize the effect of periodic boundary conditions [17]. However, this would constrain the dynamical range by far too much for a grid resolution that is computationally feasible. For this reason, $\alpha = 2$ is a typical choice. The wavelength of the force field is then about half of the domain size. Since the isotropy of the flow produced by the forcing increases with the degree of randomness, a relatively large number of modes should be chosen. On the other hand, higher wave numbers must not be contaminated by forcing modes. For this reason, stochastic Fourier modes are usually defined in a narrow window of wavenumbers centered around the characteristic wavenumber $k_0 = 2\pi/L = 2\pi\alpha/X$. In [8], for instance, the variance in Eq. (2.7) is given by

$$\sigma(\mathbf{k}) \propto \begin{cases} k^2(2k_0 - k)^2 & \text{if } 0 < k < 2k_0, \\ 0 & \text{if } k \geq 2k_0. \end{cases} \tag{2.8}$$

The parabolic form of $\sigma(\mathbf{k})$ corresponds to the energy spectrum $E(k) \propto k^4$ at small wave numbers, which is a common assumption for the energy-containing range.

The mix of transversal (perpendicular to $\mathbf{k}$) and longitudinal (parallel to $\mathbf{k}$) components can be adjusted by means of the projection operator

$$(P_{ij})_\zeta(\mathbf{k}) = \zeta P_{ij}^{\perp}(\mathbf{k}) + (1-\zeta) P_{ij}^{\parallel}(\mathbf{k}) = \zeta\delta_{ij} + (1-2\zeta)\frac{k_i k_j}{k^2}. \tag{2.9}$$

The parameter ζ determines the corresponding Helmholtz decomposition of the force field in physical space. If $\zeta = 1$, all modes are perpendicular to the wavevectors and the resulting force field is purely *solenoidal* (divergence-free). Solenoidal forcing (also called stirring) produces large-scale eddies. In the case $\zeta = 0$, on the other hand, projections parallel to the wave vectors results in a *dilatational* (rotation-free) field. The forcing is commonly called *compressive* in this case, although it produces both compressions ($d < 0$) and rarefactions ($d > 0$).

It is convenient to define the normalization coefficient g_ζ by

$$g_\zeta = \frac{3}{\sqrt{1 - 2\zeta + 3\zeta^2}}. \tag{2.10}$$

By using the properties of the Ornstein-Uhlenbeck process and definition (2.9), it can be shown that the root mean square (RMS) magnitude of the force in the statistically stationary regime is

$$\langle \hat{f}^2(\mathbf{k}, t)\rangle^{1/2} = \frac{3V}{T}\sigma(\mathbf{k}). \tag{2.11}$$

With an appropriate normalization of $\sigma(\mathbf{k})$, the physical force following from the inverse Fourier transform has a magnitude $\sim 3V/T$. Once turbulence reaches a steady state, the RMS velocity is about $v_{\rm rms} = \langle v^2\rangle^{1/2} \sim \sqrt{3}V$. The actual flow velocities reached in simulations tend to be less, however, because of the limited efficiency of the energy injection process, particularly if ζ is small (mainly compressive forcing).

As an illustration of the turbulent fields produced by stochastic forcing in numerical simulations with the FLASH code, projections of the density ρ, vorticity $\omega = |\nabla \times \mathbf{v}|$, and divergence $d = \nabla \cdot \mathbf{v}$ onto a plance are shown in Fig. 2.1 (see Chap. 3 and [9] for further details). In one simulation, purely solenoidal forcing ($\zeta = 1$) is applied, and in the other the forcing is compressive ($\zeta = 0$). The RMS Mach number is roughly 5 in both cases. One can see that compressive forcing produces pronounced large-scale structures with higher density contrasts in comparison to solenoidal forcing. As indicated by the vorticity, turbulence tends to be concentrated in the overdense gas in the case of compressive forcing, while vortex filaments are more uniformly distributed if the forcing is solenoidal. The shock fronts produced in the gas are associated with strongly negative divergence.

While solenoidal forcing has been used as the archetypical form of forcing ("turbulence stirring") in many simulations, mixed forcing was introduced in [16]. Supersonic turbulence simulations with dominant compressive components of the forcing [8, 9] were motivated by production mechanisms of turbulence in the interstellar medium, such as gravity-driven flows or supernova shock waves. A theoretical argument is invoked in [4]: Since compressions have a preferred direction, while eddies are two-dimensional structures, a mixture of 1/3 compressive (longitudinal) and 2/3 solenoidal (transversal) modes would be optimal (as shown in [9], this corresponds to $\zeta = 0.5$). Furthermore, it is argued in [18] that solenoidal and compressive modes should be excited in a particular ratio for a given Mach number, otherwise the turbulent cascade will be distorted by the large-scale forcing over a wide range of wavenumbers. Either viewpoint has its merits, depending one what the forcing is supposed to model. If the forcing is a crude model for the energy injection at the largest scales of the system, any mixture could be justified. In this case, however, forcing from the boundaries (e.g. the colliding-flow scenario in [19–22]) might arguably be a more realistic model. On the other hand, if the forcing mimics energy transfer from length scales greater then the computational domain, i.e., the box statistically represents a "piece" of a much larger turbulent flow, then it is plausible that the solenoidal-to-compressive ratio is fixed.

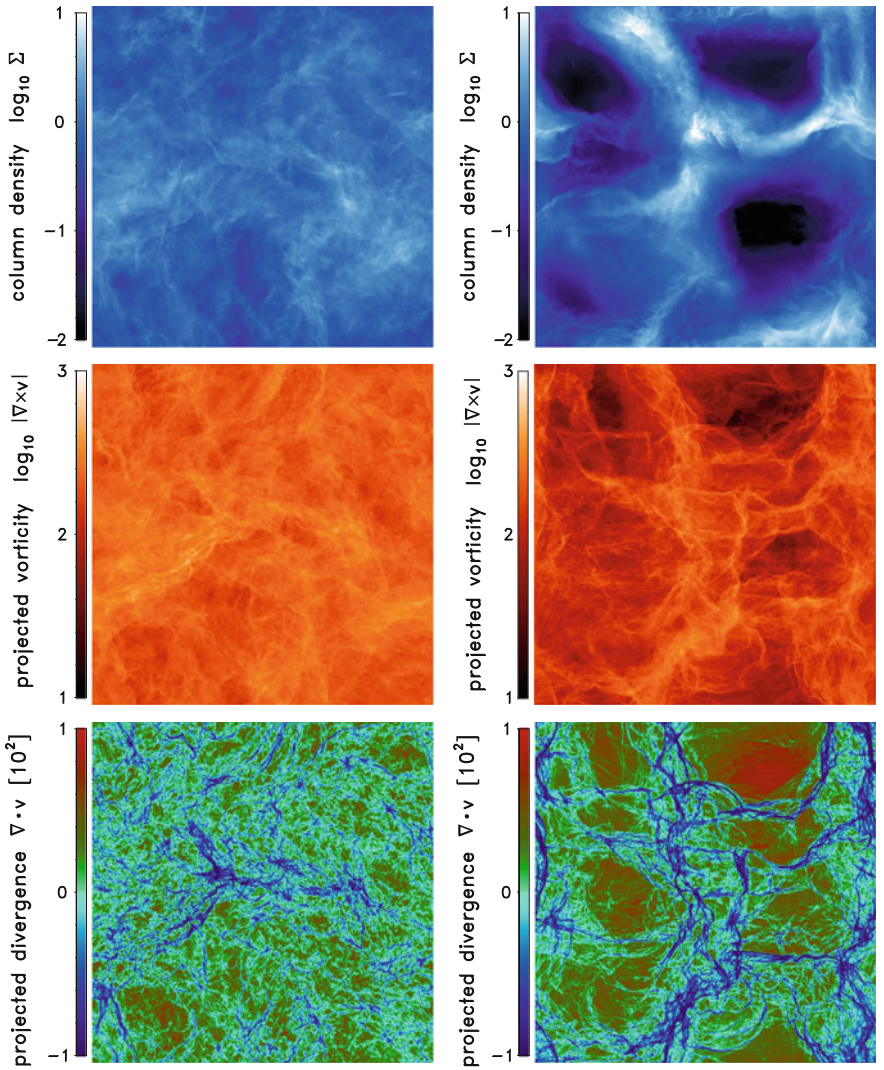

Fig. 2.1 Projections of the gas density (*top*), vorticity (*middle*) and divergence (*bottom*) at time $t = 2\,T$ in FLASH simulations with solenoidal forcing (*left*) and compressive forcing (*right*) [9]. By courtesy of Christoph Federrath

2.2 Adaptive Mesh Refinement

The basic idea of adaptive mesh refinement (AMR) is to dynamically increase the numerical resolution in regions of interest in the course of a simulation. *Block-structured* AMR works with a hierarchy of rectangular grid patches or blocks, which can be created or destroyed according to some refinement criteria [23, 24].

This method is implemented, for example, in the fluid dynamics codes ENZO [25], FLASH [26], and NYX [27]. Usually, grids patches with higher resolution than the parent grids are inserted if a given overdensity is reached or gradients of dynamical variables such as the velocity exceed given thresholds. *Tree-based* AMR codes, on the other hand, create refined regions on a cell-by-cell basis, where the cells are organized in tree structures. An example is the RAMSES code [28, 29].

While AMR is widely used for simulations of self-gravitating systems, the application to turbulence is regarded as infeasible if the turbulent structures fill most of the computational domain. Owing to the intermittency of turbulence, however, turbulent eddies or shocks at a particular instant of time occupy a volume fraction that decreases with length scale. As pointed out in [30], the number of degrees of freedom following from the β-model (see Sect. 1.3) is roughly

$$N \sim \mathrm{Re}^{3D/(D+1)}, \tag{2.12}$$

where D is interpreted as the fractal dimension of dissipative structures. If $1 < D < 2$ for compressible turbulence, then $\mathrm{Re}^{3/2} \lesssim N \lesssim \mathrm{Re}^2$. Compared to $\mathrm{Re}^{9/4}$, which follows from the estimate (1.24) for space-filling turbulence ($D = 3$), the number of degrees of freedom is significantly reduced. It is still very difficult, however, to turn this into an advantage if the limited efficiency to track complicated dynamical structures and the computational overhead of AMR are taken into account.

An essential requirement for computing turbulent flow with AMR is the sensitivity of the refinement criteria on small-scale properties of the flow. For this reason, gradients of the velocity, the density or other fields are used as so-called control variables. The simplest option is to prescribe fixed thresholds for the gradients. It is generally difficult, however, to choose thresholds such that the refinement is efficient (small filling factor of refined regions), while it is guaranteed that all turbulent structures are tracked down (high filling factor). An example are the AMR simulations of galaxy clusters in [31]: To increase the resolution in the vicinity of shocks, refinement is triggered if the difference between the velocities in adjacent cells becomes greater than a given fraction of the local velocity magnitude. However, this introduces a dependence on the motion of the frame of reference and the spatial orientation of the coordinate axes. This can be avoided by using *structural invariants*, i.e., scalars derived from the velocity gradient. A natural choice to track down turbulent eddies is the vorticity modulus ω:

$$q_1 = \frac{1}{2}\omega^2 = \frac{1}{2}|\nabla \times \mathbf{v}|^2 \tag{2.13}$$

Since the steepening of density gradients in the vicinity of shocks is associated with rapidly increasing gas compression, the rate of compression is proposed as additional control variable in [8]. For isothermal gas (see Eqs. 1.69 and 1.75),

$$q_2 = -\frac{\mathrm{D}d}{\mathrm{D}t} = \frac{1}{2}\left(|S|^2 - \omega^2\right) + c_\mathrm{s}^2\nabla^2 s \tag{2.14}$$

if the gravity and forcing terms are neglected.

To avoid tunable parameters, statistical moments of the control variables are used in [8] to define the thresholds for refinement. Since the typical magnitude of fluctuations is given by the standard deviation $\mathrm{std}\, q_i(t)$, where

$$\mathrm{std}^2 q_i(t) = \langle q_i^2(\mathbf{x}, t)\rangle - \langle q_i(\mathbf{x}, t)\rangle^2, \tag{2.15}$$

a grid cell is flagged for refinement if any of the control variable deviates by more than one standard deviation from its mean value. Thus, the refinement criterion is

$$q_i' = q_i - \langle q_i(\mathbf{x}, t)\rangle \geq \mathrm{thresh}\, q_i(t), \tag{2.16}$$

where the threshold is defined by

$$\mathrm{thresh}\, q_i(t) := \max\left[\langle q_i(\mathbf{x}, t)\rangle, \mathrm{std}\, q_i(t)\right]. \tag{2.17}$$

This definition ensures that refinement is only triggered by pronounced fluctuations. For a nearly uniform field with $q_i'(\mathbf{x}, t) \ll \langle q_i(\mathbf{x}, t)\rangle$, refinement is inhibited. Only if the mean value is small, for example, in the initial phase, an absolute lower bound has to be specified. For strongly fluctuating fields, the refinement criterion effectively becomes $q_i'(\mathbf{x}, t) \geq \mathrm{std}\, q_i(t)$. Except for the root grid, for which global averages are calculated, the averaging is constrained to the refined regions at higher levels.

As an example, we consider an AMR simulation of supersonic isothermal turbulence performed with ENZO (see Chap. 3 and [8] for further details). The initial grid (also called the *root grid*) has a resolution of $N_0 = 196^3$. Based on the refinement criteria defined above, refined grids with four times smaller cells are inserted, which results in the effective resolution $N_{1,\mathrm{eff}} = 768^3$. Turbulence is produced by stochastic forcing with $\zeta = 0.1$, as described in Sect. 2.1. Slices of the mass density and the local Mach number of the flow in this simulation are plotted for different instants of time in Figs. 2.2 and 2.3. The mainly compressive forcing produces converging gas streams in random directions. At the interfaces in between these streams, the gas is strongly compressed and shock fronts are forming. As one can see in Fig. 2.2, the shock-compressed gas is very well tracked by AMR, while smooth regions remain coarse. Figure 2.3 shows the onset of turbulence due to instabilities at the collision interfaces. These structures are also covered by refined regions.

A quantitative indicator for the reliability of AMR are probability density functions (PDFs; see Sect. 1.2.2). Figures 2.4, 2.5 and 2.6 compare PDFs of the mass density, the vorticity modulus, and divergence after one dynamical time scale for AMR and a static-grid simulation with uniform grid resolution $N_0 = 768^3$. The agreement between the PDFs from these two simulations is very good. In particular, the high-density and high-vorticity tails are well reproduced with refinement by vorticity (Eq. 2.13) and compression rate (Eq. 2.14). The deviations in the left tails of the PDF are expected because the refinement criteria are optimized to capture peak values, which are located in the right tails. But important effects such as high overdensities that might give rise to gravitational collapse are associated with the

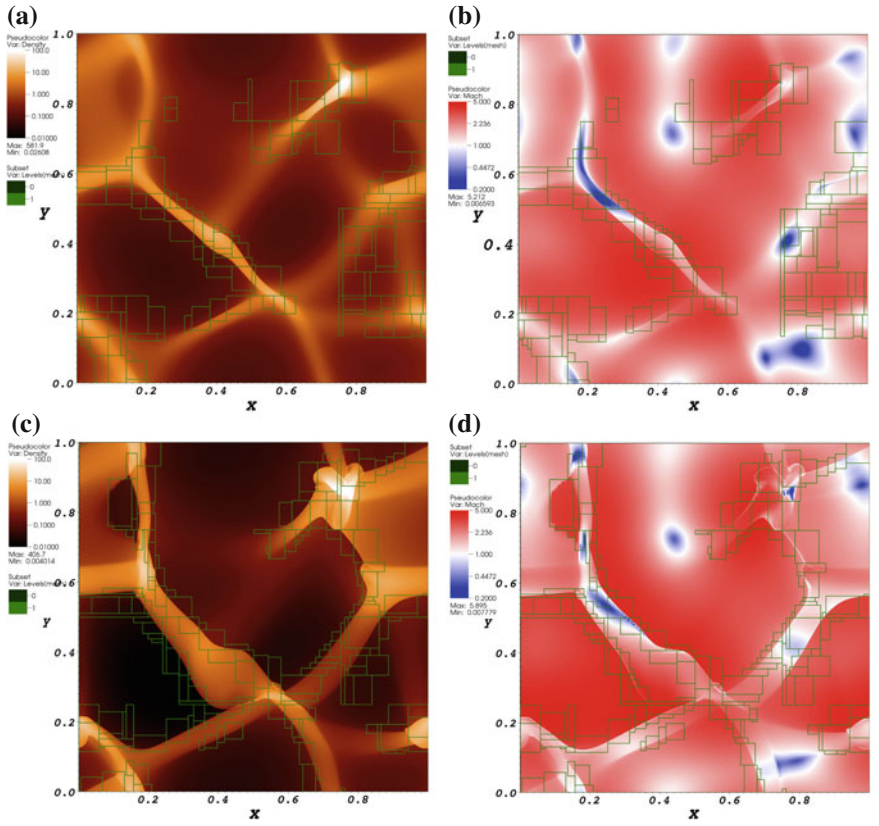

Fig. 2.2 Slices of the mass density ρ and the Mach number $\mathscr{M} = v/c_s$ in snapshots from an AMR simulation of supersonic turbulence [8]. The rectangles show the boundaries of refined grid patches **a** $\rho(t = 0.44T)$. **b** $\mathscr{M}(t = 0.44T)$. **c** $\rho(t = 0.58T)$. **d** $\mathscr{M}(t = 0.58T)$

right tails. The comparison demonstrates that, in principle, AMR can be applied to turbulence simulations, although the continuously changing grid structure is difficult to handle with sufficient efficiency. If turbulence is produced only in certain regions, however, AMR simulations can benefit from turbulence-based refinement criteria [32, 33].

2.3 Large Eddy Simulations

A common problem of astrophysical turbulence simulations are the usually very high Reynolds numbers. According to the criterion (1.24), direct numerical simulations, which encompass the full the dynamical range from the forcing length scale L to the viscous dissipation scale l_K, are infeasible. The majority of simulations are so-called

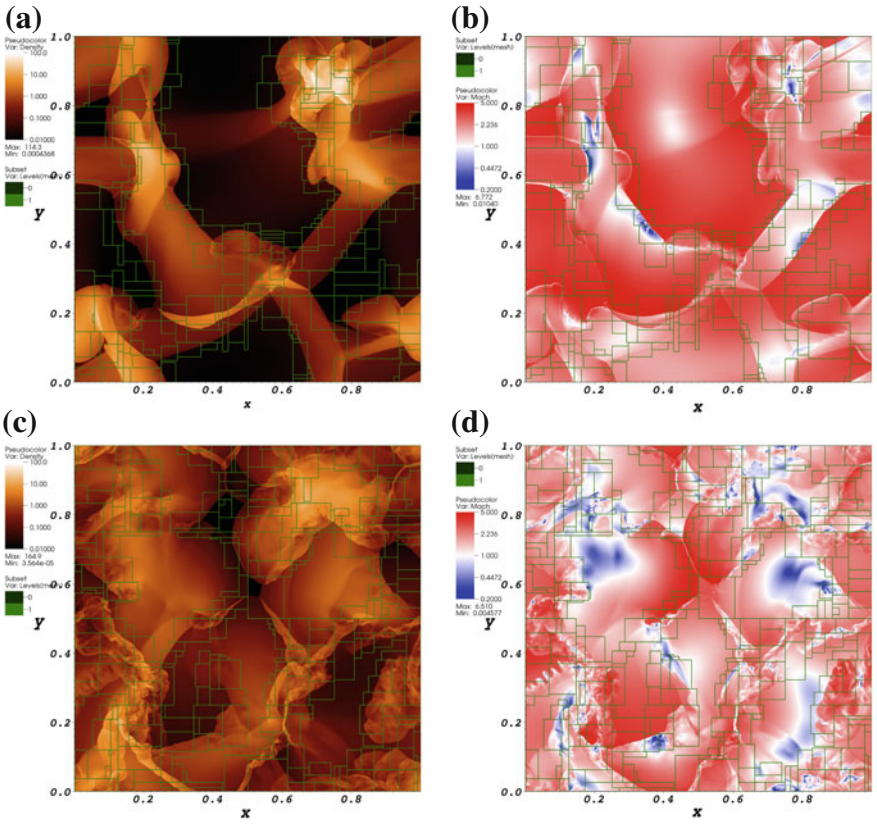

Fig. 2.3 Density and Mach number slices, continuing Fig. 2.2. **a** $\rho(t = 0.73T)$. **b** $\mathscr{M}(t = 0.73T)$. **c** $\rho(t = 1.02T)$. **d** $\mathscr{M}(t = 1.02T)$

implicit large eddy simulation (ILES). This means that the numerical viscosity associated with the truncation terms of the numerical discretization smoothes the flow over several grid cells and dissipates kinetic energy. Consequently, the physical scale of energy dissipation l_K is replaced by the grid scale Δ and the number of degrees of freedom is reduced to the number of grid cells. For example, all simulations mentioned in Sect. 2.1 belong to this category. On the other hand, large eddy simulations (LES) in the proper sense predict the rate at which energy is transported by the turbulent cascade from numerically resolved ($l \gtrsim \Delta$) to unresolved ($l \gtrsim \Delta$) length scales [34]. LES of compressible turbulence often use a subgrid scale model for the kinetic energy of numerically unresolved velocity fluctuations and the physical dissipation of energy (Eq. 1.13), which occurs on sub-resolution scales. The basic assumption of ILES is that the latter is approximated by the numerical dissipation.

To distinguish the exact solution of the compressible Navier-Stokes from the variables that are computed in LES, we use in the following the symbols $\overset{\infty}{\rho}$ for

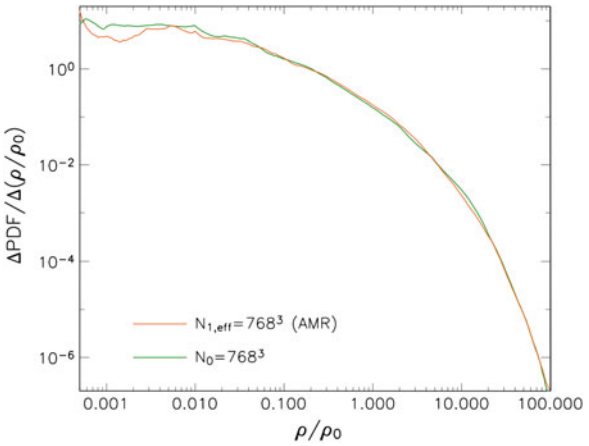

Fig. 2.4 Comparison of the probability density functions of the mass density ρ for static-grid and AMR simulations of mainly compressively driven turbulence with the same effective resolution (here, the acronym PDF in the vertical axis label signifies the probability distribution function, whose derivative is the probability density function) [8]

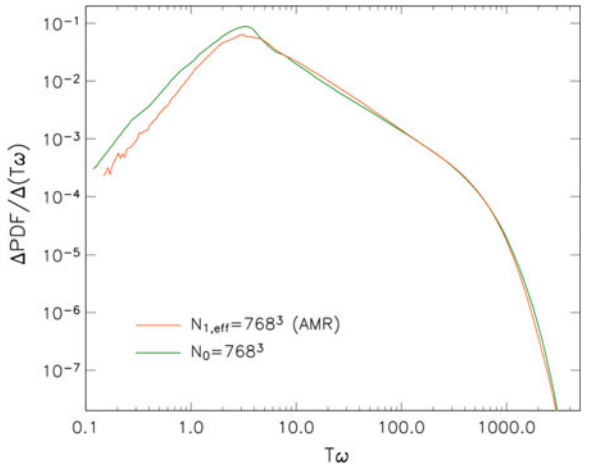

Fig. 2.5 Comparison of the probability density functions of the vorticity ω, as in Fig. 2.4

the mass density of the gas at infinite resolution, $\overset{\infty}{\mathbf{v}}$ for the exact flow velocity, etc. A consistent formulation of the dynamics on length scales $\gtrsim \Delta$ can by derived from the Navier-Stokes equations by means of the filter formalism introduced in [35]. The generalization of this formalism to compressible fluid dynamics is straightforward [36, 37]. The basic idea is to identify the numerically computed solution with the filtered variables $\rho := \langle \overset{\infty}{\rho} \rangle_\Delta$, $\mathbf{v} := \langle \overset{\infty}{\rho}\overset{\infty}{\mathbf{v}} \rangle_\Delta / \rho$, etc., where the filter operator $\langle \cdot \rangle_\Delta$ smoothes the variables $\overset{\infty}{\rho}$, $\overset{\infty}{\mathbf{v}}$, etc. over the length scale Δ. In LES, the filtering

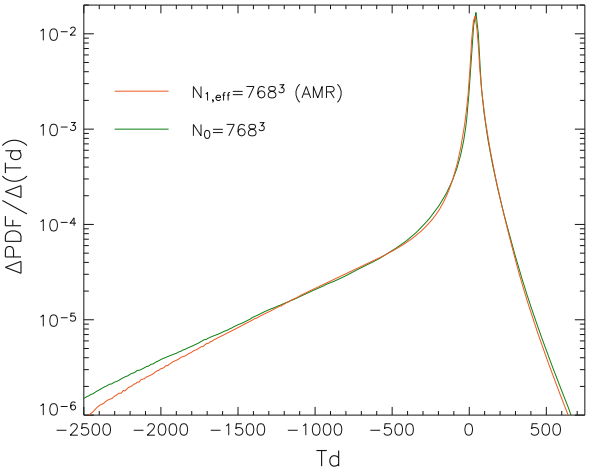

Fig. 2.6 Comparison of the probability density functions of the divergence d, as in Fig. 2.4

usually corresponds to the numerical discretization. The dynamical equations for the computable, filtered quantities are similar to the unfiltered equations, with additional terms that are related to the subgrid-scale dynamics on length scales $l < \Delta$.

Let us consider Eq. (1.2) for the momentum density of the fluid. For the exact solution, this equation reads

$$\frac{\partial}{\partial t}\left(\overset{\infty}{\rho}\overset{\infty}{\mathbf{v}}\right) + \nabla\cdot\left(\overset{\infty}{\rho}\overset{\infty}{\mathbf{v}}\otimes\overset{\infty}{\mathbf{v}}\right) = \overset{\infty}{\rho}\left(\overset{\infty}{\mathbf{g}}+\overset{\infty}{\mathbf{f}}\right) - \nabla\overset{\infty}{P} + \nabla\cdot\overset{\infty}{\sigma}, \tag{2.18}$$

where the viscous dissipation tensor $\overset{\infty}{\sigma}$ is given by

$$\overset{\infty}{\sigma}_{ij} = 2\nu\overset{\infty}{\rho}\left(\overset{\infty}{S}_{ij} - \frac{1}{3}\overset{\infty}{d}\,\delta_{ij}\right). \tag{2.19}$$

Without loss of generality, we neglect the second viscosity.

By applying a homogeneous filter operator that is uniform in time, Eq. (2.18) is converted into an equation for the filtered momentum, $\rho\mathbf{v} = \langle\overset{\infty}{\rho}\overset{\infty}{\mathbf{v}}\rangle$. This equation has the same form as the original equation, except for one term. Because of the non-linear advection term, the filtering introduces a stress term that accounts for the interaction between the numerically resolved flow and velocity fluctuations on subgrid scales:

$$\frac{\partial}{\partial t}(\rho\mathbf{v}) + \nabla\cdot(\rho\mathbf{v}\otimes\mathbf{v}) = \rho(\mathbf{g}+\mathbf{f}) - \nabla P + \nabla\cdot\left(\sigma+\tau_{\mathrm{sgs}}\right), \tag{2.20}$$

where the SGS turbulence stress tensor is defined by

$$\tau_{\mathrm{sgs}} = -\langle \overset{\infty\infty}{\rho}\,\mathbf{v} \otimes \overset{\infty}{\mathbf{v}} \rangle_{\Delta} + \rho \mathbf{v} \otimes \mathbf{v}. \tag{2.21}$$

The second-order moment $\langle \overset{\infty\infty}{\rho}\,\mathbf{v} \otimes \overset{\infty}{\mathbf{v}} \rangle_{\Delta}$ is not explicitly computable in LES because the variations of the mass density $\overset{\infty}{\rho}$ and the velocity $\overset{\infty}{\mathbf{v}}$ below the grid scale are unknown. For this reason, an approximation in terms of filtered quantities has to be devised. This is the closure problem. Alternatively, $\langle \overset{\infty\infty}{\rho}\,\mathbf{v} \otimes \overset{\infty}{\mathbf{v}} \rangle_{\Delta}$ can be expressed in terms of higher-order moments, but this merely shifts the closure problem to the higher-order moments.

The SGS turbulence energy density is defined by the difference between the resolved kinetic energy and the filtered kinetic energy:

$$K_{\mathrm{sgs}} := \frac{1}{2} \langle \overset{\infty\infty}{\rho}\,\mathbf{v} \cdot \overset{\infty}{\mathbf{v}} \rangle_{\Delta} - \frac{1}{2} \rho |\mathbf{v}|^2 = -\frac{1}{2} \mathrm{tr}\, \tau_{\mathrm{sgs}}, \tag{2.22}$$

where $\mathrm{tr}\, \tau_{\mathrm{sgs}} = \tau_{ii}$ is the trace of the SGS turbulence stress tensor (the components of τ_{sgs} are simply denoted by τ_{ij}). On the right-hand side of Eq. (2.20), the contribution from the trace corresponds to the term $-\frac{2}{3} \nabla K_{\mathrm{sgs}}$. This term can be absorbed into the pressure gradient if the thermal pressure P is replaced by the effective pressure

$$P_{\mathrm{eff}} = P + \frac{2}{3} K_{\mathrm{sgs}} = P - \frac{1}{3} \mathrm{tr}\, \tau_{\mathrm{sgs}}. \tag{2.23}$$

The relative contribution of the turbulent pressure $P_{\mathrm{sgs}} = \frac{2}{3} K_{\mathrm{sgs}}$ compared to the thermal pressure P is characterized by the SGS turbulence Mach number

$$\mathscr{M}_{\mathrm{sgs}} = \left(\frac{2 K_{\mathrm{sgs}}}{\rho c_{\mathrm{s}}^2} \right)^{1/2}, \tag{2.24}$$

where c_{s} is the thermal speed of sound. $\mathscr{M}_{\mathrm{sgs}}$ depends on the temperature of the fluid and the cutoff scale Δ. The dependence on Δ is investigated in Sect. 3.4.

The SGS turbulence energy is an intermediate reservoir of energy that exchanges energy with the resolved flow and loses energy through dissipation into heat. For the computation of K_{sgs}, the following partial differential equation has to be solved in addition to the filtered equations for the numerically resolved gas dynamics:

$$\frac{\partial}{\partial t} K_{\mathrm{sgs}} + \nabla \cdot (\mathbf{v} K_{\mathrm{sgs}}) = \Gamma + \Sigma - \rho(\varepsilon + \lambda) + \mathfrak{D}. \tag{2.25}$$

Here, $\Sigma = \tau_{ij} S_{ij}$ is the rate of SGS turbulence energy production by the turbulent cascade (also called the *turbulence energy flux*) and $\rho\varepsilon$ is the viscous dissipation rate smoothed over the grid scale. Effects caused by SGS fluctuations of the gravitational potential and the thermal pressure are given by Γ and $\rho\lambda$, respectively. The term $\mathfrak{D}$ accounts for SGS transport effects. Exact definitions of these terms are given

in [36]. For our purpose it is sufficient to discuss closures of these terms, which are approximations in terms of the numerically resolved variables and $K_{\rm sgs}$.

To compute the SGS turbulence stress tensor (2.21) in the highly compressible regime, the following closure is proposed in [37]:

$$\tau_{ij} = 2C_1\Delta(2\rho K_{\rm sgs})^{1/2}S^*_{ij} - 2C_2K_{\rm sgs}\frac{2v_{i,k}v_{j,k}}{|\nabla\otimes\mathbf{v}|^2} - \frac{2}{3}(1-C_2)K_{\rm sgs}\delta_{ij}. \qquad (2.26)$$

where $|\nabla\otimes\mathbf{v}| := (2v_{i,k}v_{i,k})^{1/2}$ is the norm of the resolved velocity derivative, $S^*_{ij} = S_{ij} - \frac{1}{3}d\delta_{ij}$ the trace-free part of S_{ij}, and d the divergence. The first term in Eq. (2.26) corresponds to the *eddy-viscosity closure*, which is commonly used for LES of weakly compressible turbulence [38]. The second term, which is non-linear in the velocity gradient, was originally applied to decaying adiabatic turbulence [39]. The standard eddy-viscosity closure with the turbulent viscosity

$$\nu_{\rm sgs} = C_1\Delta(2K_{\rm sgs}/\rho)^{1/2} \qquad (2.27)$$

follows for $C_2 = 0$. In general, the linear eddy-viscosity term dominates if $(K_{\rm sgs}/\rho)^{1/2}$ is small compared to $\Delta|S^*| \lesssim \Delta|\nabla\otimes\mathbf{v}|$. For strong turbulence intensity, i. e., $(K_{\rm sgs}/\rho)^{1/2} \gtrsim \Delta|\nabla\otimes\mathbf{v}|$, the non-linear term contributes significantly. This particularly applies to intermittent events in supersonic turbulence, for which $\Delta|\nabla\otimes\mathbf{v}| \gtrsim c_{\rm s}$. Independent of the values of C_1 and C_2, $\tau_{ii} = -2K_{\rm sgs}$, as required by the identity (2.22). The trace-free part of the SGS turbulence stress tensor is denoted by τ^*_{ij}. In Sect. 3.4.1, the eddy-viscosity and non-linear contributions to the closure (2.26) are analyzed for supersonic turbulence.

The viscous stresses $\overset{\infty}{\sigma}_{ij}$ dissipate kinetic energy on the smallest dynamical length scales $l \sim l_{\rm K}$ of the physical flow $\overset{\infty}{\mathbf{v}}$. The length scale $l_{\rm K}$ is called the Kolmogorov scale. The corresponding rate of energy dissipation, filtered over the grid scale Δ, is given by

$$\rho\varepsilon = \langle\overset{\infty}{\sigma}_{ij}\overset{\infty}{v}_{i,j}\rangle_\Delta = \langle 2\nu\overset{\infty}{\rho}\overset{\infty}{S}^*_{ij}\overset{\infty}{S}^*_{ij}\rangle_\Delta = \langle\nu\overset{\infty}{\rho}|\overset{\infty}{S}^*_{ij}|^2\rangle_\Delta. \qquad (2.28)$$

It is important to note that $\rho\varepsilon \neq \sigma_{ij}v_{i,j}$, where σ_{ij} and $v_{i,j}$ are the filtered viscous stress tensor and the filtered velocity gradient, respectively. For fully developed incompressible turbulence, simple scaling arguments based on Eq. (1.24) show that the viscous stress term in the filtered momentum equation (2.20) is negligible if $l_{\rm K} \ll \Delta$, i. e., $|\sigma| \ll |\tau_{\rm sgs}|$ [40]. Consequently, the *physical* energy dissipation occurs entirely on subgrid scales $l \sim l_{\rm K} \ll \Delta$. However, this does not imply that the rate of energy dissipation $\rho\varepsilon$ defined by Eq. (2.28) vanishes. In the limit $l_{\rm K}/\Delta \to 0$, velocity fluctuations on ever smaller length scales give rise to arbitrarily steep velocity gradients, which add up to a non-vanishing product of the viscosity times the squared rate of strain, regardless of how small the viscosity is. This results in a non-zero, asymptotically constant mean rate of energy dissipation, which is supported by experimental and numerical evidences [41, 42]. LES of supersonic turbulence suggest that this assumption holds even for supersonic turbulence (see Sect. 3.4).

If we assume that SGS turbulence energy is dissipated into heat at a rate proportional to $K_{\rm sgs}$ divided by the time scale $\Delta(K_{\rm sgs}/\rho)^{-1/2}$, the following closure for the dissipation rate is obtained:

$$\rho\varepsilon = C_\varepsilon \frac{K_{\rm sgs}^{3/2}}{\rho^{1/2}\Delta}. \tag{2.29}$$

In the case of supersonic turbulence, however, no satisfactory closes are available for the pressure-dilatation $\rho\lambda$. The simplest solution is to neglect pressure dilatation [39]. The transport term in Eq. (2.25) can be modelled by the gradient-diffusion approximation [38]

$$\mathfrak{D} = \nabla\cdot\left[\kappa_{\rm sgs}\nabla\left(\frac{K_{\rm sgs}}{\rho}\right)\right], \tag{2.30}$$

where the SGS turbulent diffusivity is approximated by $\kappa_{\rm sgs} \approx 0.65\Delta(\rho K_{\rm sgs})^{1/2}$, as shown in [36].

Furthermore, we assume that the self-gravity of the gas has no significant effects on length scales below the grid resolution. Then $\Gamma = 0$ in Eq. (2.25). This corresponds to the condition that the local Jeans length $\lambda_{\rm J} = c_{\rm s}(\pi/G\rho)^{1/2}$ (see Sect. 1.4) is sufficiently large compared to the grid scale Δ, a condition that is usually satisfied in astrophysical simulations [43–45]. Therefore, the filtered equations of fluid dynamics resulting from the compressible Navier-Stokes equations in the limit of $l_{\rm K} \ll \Delta$ read [36]

$$\frac{\partial}{\partial t}\rho + \nabla\cdot(\mathbf{v}\rho) = 0, \tag{2.31}$$

$$\frac{\partial}{\partial t}(\rho\mathbf{v}) + \nabla\cdot(\rho\mathbf{v}\otimes\mathbf{v}) = \rho(\mathbf{g}+\mathbf{f}) - \nabla(P + P_{\rm sgs}) + \nabla\cdot\tau^*_{\rm sgs}, \tag{2.32}$$

$$\frac{\partial}{\partial t}E_{\rm tot} + \nabla\cdot(\mathbf{v}E_{\rm tot}) = \rho\mathbf{v}\cdot(\mathbf{g}+\mathbf{f}) - \nabla\cdot[\mathbf{v}(P+P_{\rm sgs})] + \nabla\cdot(\mathbf{v}\cdot\tau^*_{\rm sgs}) - \Sigma + \rho\varepsilon. \tag{2.33}$$

The numerically resolved energy density is $E_{\rm tot} = \rho e_{\rm tot}$, where $e_{\rm tot}$ is defined by Eq. (1.5). Since the resolved velocity $\mathbf{v}$ is unaffected by the physical viscosity on length scales $l \geq \Delta$, the above set of equations defines the compressible *Euler* equations for computational fluid dynamics in a physically meaningful and consistent way. These equations are supplemented by the equation of state (1.6), the SGS turbulence energy equation (2.25), and the Poisson equation for the gravitational potential (1.9). The pure compressible Euler equations without SGS terms, on the other hand, do not follow from the compressible Navier-Stokes equation in the limit of infinite Reynolds number. In this case, there is no viscous dissipation at all and, by definition, ε vanishes identically. This is a mathematical idealization that does not describe turbulent flows in nature.

ILES follow as a special case from the above approach if two basic assumptions are made. Firstly, the discretization of the compressible Euler equations introduces

a dissipative leading error term $\mathfrak{D}_{\text{num}}$ in the momentum equation (2.31). Implicitly, this term is assumed to be equivalent to the SGS turbulence stress term $\nabla \cdot \tau_{\text{sgs}}$. The second assumption is that $\mathbf{v} \cdot \mathfrak{D}_{\text{num}} = -\rho\varepsilon$, i.e., kinetic energy on the resolved scales is directly dissipated into heat at a rate that approximates the viscous dissipation on unresolved length scales. This is referred to as numerical viscosity or numerical dissipation. Effectively, the following equations are solved in ILES:

$$\frac{\partial}{\partial t}\rho + \nabla \cdot (\mathbf{v}\rho) = 0, \tag{2.34}$$

$$\frac{\partial}{\partial t}(\rho\mathbf{v}) + \nabla \cdot (\rho\mathbf{v} \otimes \mathbf{v}) = \rho(\mathbf{g} + \mathbf{f}) - \nabla P + \mathfrak{D}_{\text{num}}, \tag{2.35}$$

$$\frac{\partial}{\partial t}E_{\text{tot}} + \nabla \cdot (\mathbf{v}E_{\text{tot}}) = \rho\mathbf{v} \cdot (\mathbf{g} + \mathbf{f}) - \nabla \cdot (\mathbf{v}P). \tag{2.36}$$

Despite the lack of a strict mathematical justification, ILES serves as a very useful approximation in numerous astrophysical applications. Many properties of compressible turbulence are investigated with ILES. Moreover, numerical dissipation in addition to the explicit dissipation defined by Eq. (2.29) cannot be avoided in LES if numerical schemes for compressible fluid dynamics such as the piecewise parabolic method (PPM) are applied.

As an example, Fig. 2.7 shows a visualization of K_{sgs} from an LES of supersonic turbulence with a resolution of 512^3 grid cells [37]. The parameters of this simulation were chosen to match the ILES with solenoidal forcing presented in Sect. 2.1. An LES with purely compressive forcing is shown Fig. 2.8. In both cases, the forcing

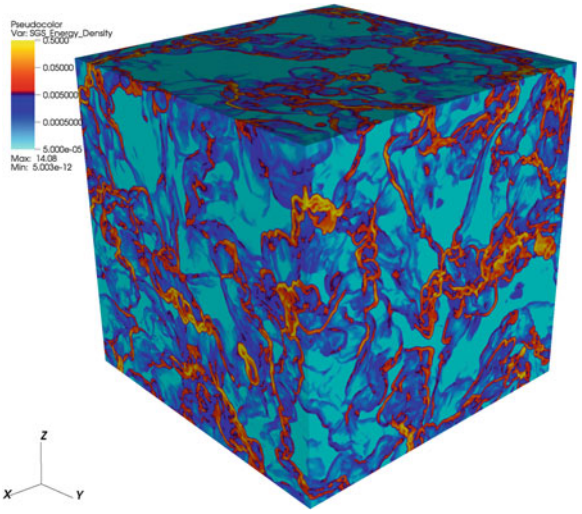

Fig. 2.7 Visualization of the SGS turbulence energy density K_{sgs} in a 512^3 LES with solenoidal forcing [37]

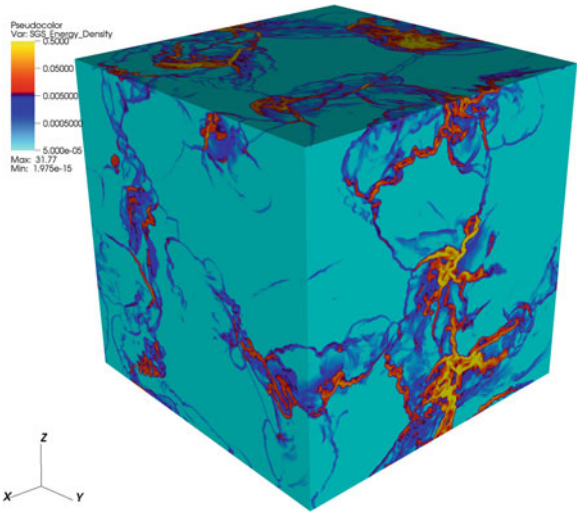

Fig. 2.8 Visualization of the SGS turbulence energy density $K_{\rm sgs}$ in a 512^3 LES with compressive forcing

magnitude was adjusted to obtain a steady-state RMS Mach number around 5. In the reddish regions of the plots, $K_{\rm sgs}$ is higher than the spatial mean, while it is lower in the bluish regions. The production of SGS turbulence energy depends on the numerically resolved turbulent velocity fluctuations. It is therefore interesting to compare $K_{\rm sgs}$ to the denstrophy $\Omega_{1/2} = \frac{1}{2}\left|\nabla \times \left(\rho^{1/2}\mathbf{u}\right)\right|^2$, which was proposed as an indicator of compressible turbulent velocity fluctuations [4]. The correlation diagrams of $K_{\rm sgs}$ versus $\Delta^2\Omega_{1/2}$ in Fig. 2.9 show that, on the average, $K_{\rm sgs} \sim 0.1\Delta^2\Omega_{1/2}$ for relatively large denstrophy values. Locally, however, $K_{\rm sgs}$ and $\Delta^2\Omega_{1/2}$ can substantially deviate from the average relation. This is a consequence of the different processes contributing to the SGS dynamics, which are not fully encompassed by the derivative of the resolved velocity field. For this reason, derived quantities such as the rate of strain or the denstrophy are only of limited utility to estimate effects of turbulence on unresolved length scales.

The effective pressure (2.23) is plotted versus the mass density in Fig. 2.10. One can see that the average of the effective pressure for a given mass density closely follows the isothermal relation $P \propto \rho$. This is because the mean turbulent pressure $P_{\rm sgs}$ is small compared to the thermal pressure for the resolution $\Delta = L/256$. However, the intermittency of turbulence can locally produce an effective pressure that exceeds the thermal pressure by one order of magnitude. For lower numerical resolution, this effect becomes stronger. In addition to the turbulent pressure, the diffusive non-diagonal viscous stresses τ^*_{ij} act on the resolved flow (see Eq. 2.32).

The rate of energy dissipation on the grid scale is predicted by Eq. (2.29). In ILES, one could alternatively extrapolate the expression for the microscopic dissipation rate (Eq. 1.13) to the grid scale Δ. This leads to the expression

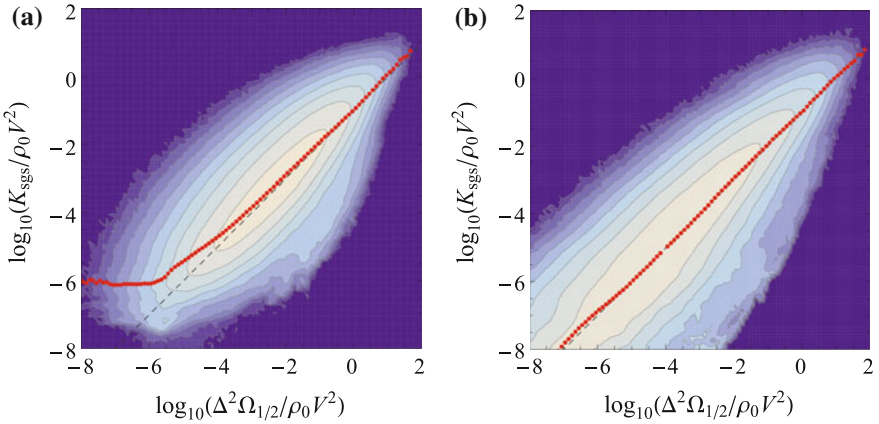

Fig. 2.9 Correlation diagrams of the SGS turbulence energy versus the denstrophy for 512^3 LES with solenoidal and compressive forcing [37]. The quantities are normalized by characteristic scales. The spacing of the contours is logarithmic. The average relation between both quantities is indicated by the *thick dotted lines*, and the *dashed line* shows the relation $K_{\rm sgs} \sim 0.1\Delta^2\Omega_{1/2}$. **a** Solenoidal. **b** Compressive

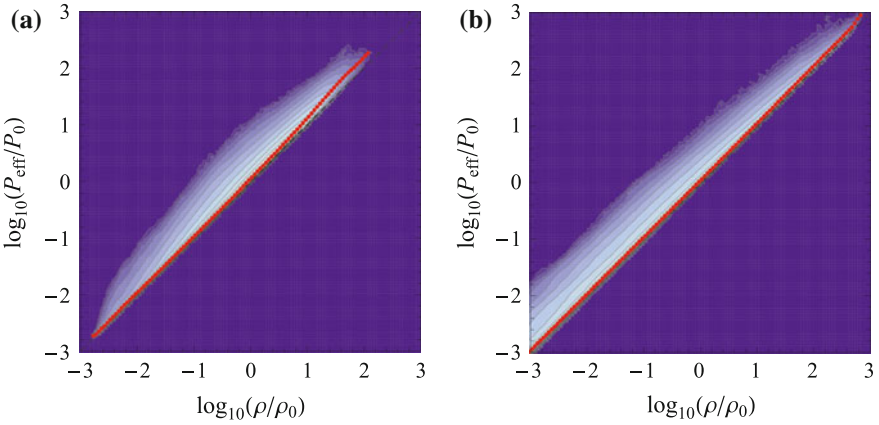

Fig. 2.10 Phase diagrams of the effective pressure defined by Eq. (2.23) versus the mass density for 512^3 LES with solenoidal and compressive forcing [37]. The averages of the SGS turbulence energy for particular values of the denstrophy are indicated by the *thick dotted lines*. **a** Solenoidal. **b** Compressive

$$\rho\varepsilon = \rho\nu_\Delta |S^*|^2, \tag{2.37}$$

where a constant numerical viscosity $\nu_\Delta = VL/{\rm Re}_\Delta$ is assumed [46]. The Reynolds number on the grid scale can be estimated from mean squared rate of strain and the

root mean square velocity: $\mathrm{Re} = 2L^2\langle|S^*|^2\rangle/v_{\mathrm{rms}}^2$.[1] The problem with this approach is that the viscosity on the grid scale, which corresponds to the eddy-viscosity (2.27) of the SGS model, cannot be assumed to be constant. Neglecting diffusion, compressibility, and the non-linear term in the SGS turbulence stress tensor (2.26), the equilibrium between production and dissipation of SGS turbulence energy in Eq. (2.25) implies

$$K_{\mathrm{sgs}} \sim \frac{C_1}{C_\varepsilon}\rho\Delta^2|S^*|^2.$$

Hence, $\varepsilon \sim (\Delta/C_\varepsilon)^2(C_1|S^*|)^3$ according to Eq. (2.29), which determines the rate of energy dissipation on the basis of the scale-separation of fluid dynamics. Comparing to Eq. (2.37), we see that $\nu_\Delta \sim \Delta^2|S^*|$, which is not constant. This is a consequence of the fact that $\rho\varepsilon \neq \sigma_{ij}u_{i,j} \propto |S^*|^2$ (see Eq. 2.28). The discrepancy becomes apparent in Fig. 2.11, which shows correlation diagrams of the rate of energy dissipation calculated via Eq. (2.37) versus ε following from the SGS model. For low values of ε, one can see an average relation close to $|S^*|^2 \propto \varepsilon^{2/3}$. This is just what follows from the above estimate of the equilibrium dissipation rate. This behavior is reasonable because the neglected contribution of the non-linear term in Eq. (2.26) is relatively small for low values of K_{sgs}.

In computational astrophysics, the LES approach outlined in this section was applied to turbulent combustion in thermonuclear supernovae and to cosmological structure formation. In the former case, an SGS model is required to determine the turbulent diffusivity, which becomes much greater than the thermal diffusivity. This

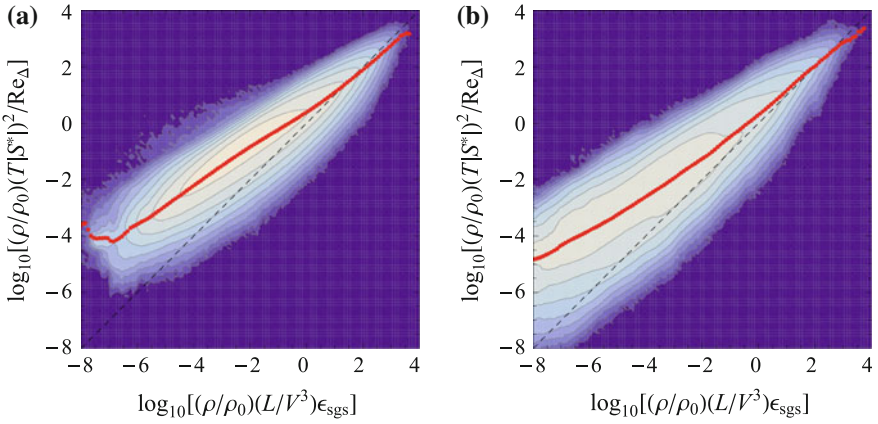

Fig. 2.11 Correlation diagrams of the normalized rate of energy dissipation defined by Eq. (2.37), where ν_Δ assumes a constant value that is given by the numerical Reynolds number, versus the rate of energy dissipation (2.29) that is predicted by the SGS model [37]. The averages of expression (2.37) for given values of $\rho\varepsilon_{\mathrm{sgs}}$ are indicated by the *thick dotted lines*. **a** Solenoidal. **b** Compressive

[1] See Eq. (3.4) in Sect. 3.1. For consistency with Eq. (2.37), however, ω_{rms}^2 is replaced by $\langle|S^*|^2\rangle = \langle\omega^2 + \frac{4}{3}d^2\rangle$.

leads to a significant enhancement of the nuclear burning rate [40, 48, 49]. To analyze the production of turbulence in simulations of cosmological structure formation, LES was combined with AMR [47, 50]. Moreover, an influence of the SGS model on the fragmentation properties of collapsing atomic cooling halos, from which the first stars in the Universe formed, is reported in [45].

References

1. R.S. Klessen, F. Heitsch, M.M. Mac Low, ApJ **535**, 887 (2000). doi:10.1086/308891
2. S. Boldyrev, A. Nordlund, P. Padoan, ApJ **573**, 678 (2002)
3. J. Ballesteros-Paredes, A. Gazol, J. Kim, R.S. Klessen, A.K. Jappsen, E. Tejero, ApJ **637**, 384 (2006). doi:10.1086/498228
4. A.G. Kritsuk, M.L. Norman, P. Padoan, R. Wagner, ApJ **665**, 416 (2007). doi:10.1086/519443
5. S. Dib, A. Brandenburg, J. Kim, M. Gopinathan, P. André, ApJ **678**, L105 (2008). doi:10.1086/588608
6. R. Kissmann, J. Kleimann, H. Fichtner, R. Grauer, MNRAS **391**, 1577 (2008). doi:10.1111/j.1365-2966.2008.13974.x
7. S.S.R. Offner, R.I. Klein, C.F. McKee, ApJ **686**, 1174 (2008). doi:10.1086/590238
8. W. Schmidt, C. Federrath, M. Hupp, S. Kern, J.C. Niemeyer, A&A **494**, 127 (2009). doi:10.1051/0004-6361:200809967
9. C. Federrath, J. Roman-Duval, R.S. Klessen, W. Schmidt, M. Mac Low, A&A **512**, A81+ (2010). doi:10.1051/0004-6361/200912437
10. D.C. Collins, A.G. Kritsuk, P. Padoan, H. Li, H. Xu, S.D. Ustyugov, M.L. Norman, ApJ **750**, 13 (2012). doi:10.1088/0004-637X/750/1/13
11. C. Federrath, R.S. Klessen, ApJ **761**, 156 (2012). doi:10.1088/0004-637X/761/2/156
12. E. Saury, M.A. Miville-Deschênes, P. Hennebelle, E. Audit, W. Schmidt, ArXiv e-prints (2013)
13. M.M. Mac Low, R.S. Klessen, A. Burkert, M.D. Smith, Phys. Rev. Lett. **80**, 2754 (1998)
14. J.M. Stone, E.C. Ostriker, C.F. Gammie, ApJ **508**, L99 (1998). doi:10.1086/311718
15. V. Eswaran, S.B. Pope, Comp. Fluids. **16**, 257 (1988)
16. W. Schmidt, W. Hillebrandt, J.C. Niemeyer, Comp. Fluids **35**, 353 (2006)
17. P.A. Davidson, *Turbulence: An Introduction for Scientists and Engineers* (Oxford University Press, Oxford, 2004)
18. A.G. Kritsuk, S.D. Ustyugov, M.L. Norman, P. Padoan, in Numerical modeling of space plasma flows, Astronum-2009, ed. by N.V. Pogorelov, E. Audit, G.P. Zank. *Astronomical Society of the Pacific Conference Series*, vol. 429. (San Francisco: Astronomical Society of the Pacific), p. 15 (2010)
19. R. Walder, D. Folini, A&AS **274**, 343 (2000). doi:10.1023/A:1026597318472
20. F. Heitsch, A.D. Slyz, J.E.G. Devriendt, L.W. Hartmann, A. Burkert, ApJ **648**, 1052 (2006). doi:10.1086/505931
21. E. Vázquez-Semadeni, G.C. Gómez, A.K. Jappsen, J. Ballesteros-Paredes, R.F. González, R.S. Klessen, ApJ **657**, 870 (2007). doi:10.1086/510771
22. P. Hennebelle, R. Banerjee, E. Vázquez-Semadeni, R.S. Klessen, E. Audit, A&A **486**, L43 (2008). doi:10.1051/0004-6361:200810165
23. M.J. Berger, J. Oliger, J. Chem. Phys. **53**, 484 (1984)
24. M.J. Berger, P. Colella, J. Chem. Phys. **82**, 64 (1989). doi:10.1016/0021-9991(89)90035-1
25. B.W. O'Shea, G. Bryan, J. Bordner, M.L. Norman, T. Abel, R. Harkness, A. Kritsuk, in Adaptive mesh refinement—theory and applications, ed. by T. Plewa, T. Linde, V.G. Weirs. *Lecture Notes in Computational Science and Engineering*, vol. 41 (Springer, Berlin, 2004), p. 341. http://esoads.eso.org/abs/2004astro.ph.3044O
26. B. Fryxell, K. Olson, P. Ricker, F.X. Timmes, M. Zingale, D.Q. Lamb, P. MacNeice, R. Rosner, J.W. Truran, H. Tufo, ApJS **131**, 273 (2000). doi:10.1086/317361

27. A.S. Almgren, J.B. Bell, M.J. Lijewski, Z. Lukić, E. Van Andel, ApJ **765**, 39 (2013). doi:10.1088/0004-637X/765/1/39
28. R. Teyssier, A&A **385**, 337 (2002). doi:10.1051/0004-6361:20011817
29. S. Fromang, P. Hennebelle, R. Teyssier, A&A **457**, 371 (2006). doi:10.1051/0004-6361:20065371
30. A.G. Kritsuk, M.L. Norman, P. Padoan, ApJ **638**, L25 (2006). doi:10.1086/500688
31. F. Vazza, G. Brunetti, A. Kritsuk, R. Wagner, C. Gheller, M. Norman, A&A **504**, 33 (2009). doi:10.1051/0004-6361/200912535
32. L. Iapichino, J. Adamek, W. Schmidt, J.C. Niemeyer, MNRAS **388**, 1079 (2008). doi:10.1111/j.1365-2966.2008.13137.x
33. S. Paul, L. Iapichino, F. Miniati, J. Bagchi, K. Mannheim, ApJ **726**, 17 (2011). doi:10.1088/0004-637X/726/1/17
34. S.B. Pope, *Turbulent Flows* (Cambridge University Press, Cambridge, 2000)
35. M. Germano, J. Fluid Mech. **238**, 325 (1992)
36. W. Schmidt, J.C. Niemeyer, W. Hillebrandt, A&A **450**, 265 (2006). doi:10.1051/0004-6361:20053617
37. W. Schmidt, C. Federrath, A&A **528**, A106+ (2011). doi:10.1051/0004-6361/201015630
38. P. Sagaut, *Large eddy simulation for incompressible flows: an introduction* (Springer, Berlin, 2006)
39. P.R. Woodward, D.H. Porter, S. Anderson, T. Fuchs, F. Herwig, J. Phys. Conf. Ser. **46**, 370 (2006). doi:10.1088/1742-6596/46/1/052
40. F.K. Röpke, W. Schmidt, in Interdisciplinary aspects of turbulence, ed. by W. Hillebrandt, F. Kupka, *Lecture Notes in Physics*, vol. 756. (Springer, Berlin, 2009), pp. 255-+
41. U. Frisch, *Turbulence. The legacy of A.N. Kolmogorov* (Cambridge University Press, Cambridge, 1995)
42. T. Ishihara, T. Gotoh, Y. Kaneda, Ann. Rev. Fluid Mech. **41**, 165 (2009). doi:10.1146/annurev.fluid.010908.165203
43. J.K. Truelove, R.I. Klein, C.F. McKee, J.H. Holliman II, L.H. Howell, J.A. Greenough, ApJ **489**, L179 (1997). doi:10.1086/316779
44. C. Federrath, S. Sur, D.R.G. Schleicher, R. Banerjee, R.S. Klessen, ApJ **731**, 62 (2011). doi:10.1088/0004-637X/731/1/62
45. M.A. Latif, D.R.G. Schleicher, W. Schmidt, J. Niemeyer, MNRAS **430**, 588 (2013). doi:10.1093/mnras/sts659
46. L. Pan, P. Padoan, A.G. Kritsuk, Phys. Rev. Lett. **102**(3), 034501 (2009). doi:10.1103/PhysRevLett.102.034501
47. L. Iapichino, W. Schmidt, J.C. Niemeyer, J. Merklein, MNRAS **414**, 2297 (2011). doi:10.1111/j.1365-2966.2011.18550.x
48. W. Schmidt, J.C. Niemeyer, W. Hillebrandt, F.K. Röpke, A&A **450**, 283 (2006). doi:10.1051/0004-6361:20053618
49. F.K. Röpke, W. Hillebrandt, W. Schmidt, J.C. Niemeyer, S.I. Blinnikov, P.A. Mazzali, ApJ **668**, 1132 (2007). doi:10.1086/521347
50. A. Maier, L. Iapichino, W. Schmidt, J.C. Niemeyer, ApJ **707**, 40 (2009). doi:10.1088/0004-637X/707/1/40

http://www.springer.com/978-3-319-01474-6

Numerical Modelling of Astrophysical Turbulence

Schmidt, W.

2014, VIII, 90 p. 50 illus., 22 illus. in color., Softcover
ISBN: 978-3-319-01474-6